



### Special Collection:

Extreme Hydrometeorological Events Under Climate Change: Past, Present, and Future

### Key Points:

- DHW and NHW being more prevalent in mid-low latitudes while CHW showing higher frequency and severity in high-latitude regions
- ENSO shapes global patterns of heatwaves through Walker circulation anomalies, especially in tropics
- Local water-energy exchanges significantly influence heatwave development, particularly in dryland and temperate climate zones

### Supporting Information:

Supporting Information may be found in the online version of this article.

### Correspondence to:

J. Wu and M. K. Ng,  
jinwu@hku.hk;  
mng@maths.hku.hk

### Citation:

Zhang, K., Li, J., Guo, Z., Liu, S., Zhu, G., Shang, S., et al. (2025). Heatwaves on the rise: The role of El Niño-Southern Oscillation and local water-energy exchanges in shaping global patterns. *Journal of Geophysical Research: Atmospheres*, 130, e2024JD042446. <https://doi.org/10.1029/2024JD042446>

Received 10 SEP 2024

Accepted 24 AUG 2025

### Author Contributions:

**Conceptualization:** Kun Zhang, Michael K. Ng, Jin Wu

**Formal analysis:** Kun Zhang, Zhengfei Guo

**Methodology:** Kun Zhang, Jinbao Li, Shuwen Liu, Jin Wu

**Project administration:** Jin Wu

**Supervision:** Michael K. Ng

**Visualization:** Kun Zhang

**Writing – original draft:** Kun Zhang

© 2025. The Author(s).

This is an open access article under the terms of the [Creative Commons Attribution License](#), which permits use, distribution and reproduction in any medium, provided the original work is properly cited.

## Heatwaves on the Rise: The Role of El Niño-Southern Oscillation and Local Water-Energy Exchanges in Shaping Global Patterns

Kun Zhang<sup>1,2</sup> , Jinbao Li<sup>3</sup> , Zhengfei Guo<sup>1</sup>, Shuwen Liu<sup>1</sup>, Gaofeng Zhu<sup>4</sup> , Shasha Shang<sup>5</sup> , Jie Zhang<sup>1</sup>, Michael K. Ng<sup>2</sup>, and Jin Wu<sup>1,6</sup>

<sup>1</sup>School of Biological Sciences and Institute for Climate and Carbon Neutrality, The University of Hong Kong, Hong Kong SAR, China, <sup>2</sup>Department of Mathematics, The University of Hong Kong, Hong Kong SAR, China, <sup>3</sup>Department of Geography, The University of Hong Kong, Hong Kong SAR, China, <sup>4</sup>College of Earth and Environmental Sciences, Lanzhou University, Lanzhou, China, <sup>5</sup>Tianjin Key Laboratory of Water Resources and Environment, Tianjin Normal University, Tianjin, China, <sup>6</sup>State Key Laboratory of Agrobiotechnology, Chinese University of Hong Kong, Hong Kong SAR, China

**Abstract** Large-scale and intense heatwaves pose significant risks to ecosystems and human society due to associated heat and water stress. Heatwaves can be classified as daytime, nighttime, and compound, depending on their occurrence time. However, the factors shaping global spatiotemporal patterns of heatwaves remain poorly understood, especially regarding links to large-scale climate mode and local water-energy (LWE) exchange. Here, we analyzed the frequency and intensity of these three heatwave types from 1980 to 2022 using ERA5L air temperature data and examined their associations with the El Niño–Southern Oscillation (ENSO) and LWE-related factors through the LSTM model. Our results show a significant global increase in all types of heatwaves. Compound heatwaves exhibited higher annual frequency and intensity than individual daytime or nighttime events. The three types of heatwaves displayed distinct associations with El Niño and La Niña episodes, with the tropics experiencing the most frequent and intense heatwaves during El Niño years. Meanwhile, terrestrial LWE exchange significantly influenced heatwave development, with stronger effects in dryland and temperate zones than in continental and polar regions. These findings highlight the importance of ENSO and LWE exchanges in shaping heatwave patterns and suggest that future forecasts should consider the temporal evolution and fluctuations in heat accumulation to improve accuracy and reliability.

**Plain Language Summary** Heatwaves, which are prolonged periods of extreme heat, are becoming increasingly severe and frequent, posing serious threats to both ecosystems and human societies. These events can occur during the day, night, or span both periods, known as compound heatwaves. Analyzing data from 1980 to 2022, we have noticed a significant rise in all types of heatwave occurrences globally, with compound heatwaves being notably more common and intense. The study also explored how these heatwaves are linked to climate patterns such as the El Niño–Southern Oscillation (ENSO), discovering that tropical regions face the most severe heatwaves during El Niño years. Additionally, local factors such as water and energy exchanges on the land surface were found to have significant impacts on how these heatwaves develop, especially in dry and temperate climates. This study underlines the importance of understanding both global climate influences and local environmental conditions to better predict and manage the risks associated with heatwaves.

## 1. Introduction

Heatwaves, characterized by prolonged periods of abnormally high air temperatures near the land surface, are a significant type of climate extreme (Russo et al., 2015). With continuing global warming, heatwaves are expected to become more frequent and intense (Luo & Lau, 2021; Meehl & Tebaldi, 2004; Perkins-Kirkpatrick & Lewis, 2020). These extreme events have considerable impacts on ecosystems and human health. For instance, heatwaves caused over 166,000 deaths globally between 1998 and 2017 (Mizutori & Guha-Sapir, 2017), and the number of fatalities and affected regions is projected to increase with global warming (Kovats & Hajat, 2008; Wouters et al., 2022). The record-breaking 2003 European heatwave caused massive heat stress of terrestrial ecosystems, which not only reduced gross primary productivity (GPP) over Europe by around 30% but also led to economic losses due to crop failure (Brás et al., 2021) and strong anomalous net source of CO<sub>2</sub> (Ciais et al., 2005). Moreover, heatwaves increase the risk of wildfires, causing additional damage to ecosystems and air/water

**Writing – review & editing:** Kun Zhang, Jinbao Li, Zhengfei Guo, Shuwen Liu, Gaofeng Zhu, Shasha Shang, Jie Zhang, Jin Wu

quality (Bowd et al., 2019; Park Williams et al., 2013; Robinne et al., 2020). Hence, enhancing our understanding of heatwave patterns and their underlying causes is crucial for uncovering the processes driving heatwave formation, accurately evaluating and projecting heatwave effects globally and in relation to climate change, and eventually developing strategies to mitigate their impacts on ecosystems and human society.

There are two primary factors that contribute to prolonged heatwave occurrences: anomalies in the synoptic system and local land-atmosphere interactions (Miralles et al., 2014, 2019). Specifically, high temperatures can be influenced by the advection of external heat sources via warm flows (Röhlisberger & Papritz, 2023; S. Zhou & Yuan, 2023). Additionally, atmospheric blocking patterns can cause further warming due to adiabatic compression in descending air (Schaller et al., 2018). Anomalous airflows in synoptic systems are often remotely influenced by large-scale atmospheric circulation modes through dynamical teleconnections (Alexander et al., 2002; Parker et al., 2014). For example, the frequency and intensity of heatwaves in Australia are found to be predominantly controlled by the large-scale seasonal phases of the El Niño-Southern Oscillation (ENSO) (Perkins et al., 2015), a prominent interannual climate mode in the Earth system. Observational analyses also reveal strong connections between ENSO episodes and heatwave occurrences in the Northern Hemisphere, as ENSO events can trigger anomalous anticyclones and jet streams over mid-latitudes via the circum-global teleconnection (Luo & Lau, 2020). However, whether similar associations between heatwaves and ENSO events occur on a global scale remains underexplored.

On the other hand, warming can also be induced by changes in sensible heat through near-surface turbulent mixing, which is driven by land-atmosphere interactions (Röhlisberger & Papritz, 2023). This process can serve as another regulator of temperature dynamics on a local scale (Horton et al., 2016; Seneviratne et al., 2010). Solar radiation initially warms the land surface through sensible heat flow while temperature regulation is closely tied to local conditions such as water availability, cloud coverage, surface albedo, and plant functional responses (Dickinson, 1983; Teuling et al., 2010; Trenberth et al., 2009). Depending on these local conditions, increased evapotranspiration due to rising temperatures may reduce surface temperatures and mitigate or even shorten heatwave durations in wet regions. In contrast, under water-limited conditions, heightened water stress accompanying warming may decrease evapotranspiration, diminish plant-associated cooling effect, dry the atmosphere, and reduce cloud cover, ultimately resulting in elevated temperatures and prolonged heatwaves (Hirsch et al., 2019; Jyoteeshkumar reddy et al., 2021). Consequently, local water-energy (LWE) exchange plays a significant role in regulating heatwave evolution and propagation on a local scale (J. Li et al., 2021; Miralles et al., 2019; Zscheischler & Seneviratne, 2017). Despite its importance, there is a lack of global assessments of heatwave evolution influenced by LWE exchange through time series analysis, and the dominant climate zones where this effect operates remain unclear.

Recently, there has been a growing emphasis on distinguishing various types of heatwaves as they often have distinct formation mechanisms and yield different impacts on society and ecosystems (Ma, Yuan, & Li, 2022; Wang et al., 2021; Wu et al., 2023). Based on anomalies in daily maximum and minimum temperatures ( $T_{\max}$  and  $T_{\min}$ ), heatwaves can be classified into three categories (Luo et al., 2022; Wang et al., 2020): daytime heatwaves (DHW, solely  $T_{\max}$  anomalies), nighttime heatwaves (NHW, solely  $T_{\min}$  anomalies), and compound heatwaves (CHW, both  $T_{\max}$  and  $T_{\min}$  anomalies). DHW exclusively involves daytime hot extremes, which are typically characterized by significant nighttime cooling and accompanied by dry conditions. In contrast, NHW is characterized by elevated moisture levels, augmented cloud cover, and intensified downward longwave radiation (Gershunov et al., 2009; Vaidyanathan et al., 2016). Furthermore, CHW integrates the distinctive characteristics of both DHW and NHW, exhibiting more intricate synoptic conditions and typically producing more severe temperature extremes. The complexity of CHW arises from the coexistence and interaction of various atmospheric and surface mechanisms, including anomalous anticyclonic circulation, drying soils, enhanced atmospheric humidity, and modified cloud dynamics, which often involving diverse and sometimes contradictory conditions (Baldwin et al., 2019; Fischer et al., 2007; Y. Li et al., 2017; Luo et al., 2022). This results in a compounding heat effect throughout the day, posing heightened risks to human and ecosystem health by impeding recovery from previous high temperatures (Ma, Yuan, Wu, & Zeng, 2022; Wang et al., 2020). However, the extent to which these three types of heatwaves exhibit distinct responses to ENSO and LWE exchange on a global scale remains underexplored.

In this study, we first examined different types of global heatwaves using the land component of the fifth generation of European ReAnalysis (ERA5-Land, hereafter referred to ERA5L) product, a state-of-the-art reanalysis

**Table 1***Detailed Information of Gridded Data Sets Used in This Study*

Data	Variable	Category	Spatial resolution	Temporal interval	Reference
ERA5L	$T_{\max}, T_{\min}$	Reanalysis	$0.1^{\circ} \times 0.1^{\circ}$	1-hr	Muñoz-Sabater et al. (2021)
MERRA2	$T_{\max}, T_{\min}$	Reanalysis	$0.625^{\circ} \times 0.5^{\circ}$	3-hr	Gelaro et al. (2017)
JRA55	$T_{\max}, T_{\min}$	Reanalysis	$1.25^{\circ} \times 1.25^{\circ}$	6-hr	Kobayashi et al. (2015)
CPC	$T_{\max}, T_{\min}$	Station-based	$0.5^{\circ} \times 0.5^{\circ}$	Daily	Pan et al. (2019)
GLEAM	$ET, \theta$	Remote sensing	$0.25^{\circ} \times 0.25^{\circ}$	Daily	Martens et al. (2017)
MSWEP	$P$	Multi-source	$0.1^{\circ} \times 0.1^{\circ}$	Daily	Beck et al. (2019)
MSWX	$DSR, DLR, RH, WS$	Multi-source	$0.1^{\circ} \times 0.1^{\circ}$	Daily	Beck et al. (2022)

data set with  $0.1^{\circ}$  spatial resolution and hourly temporal intervals. Then, we explored the global associations between different heatwave types, ENSO episodes, and LWE exchange using statistical methods and deep learning model. The main objectives of this study include: (a) assessing the spatial and temporal trends of various heatwave types over the past four decades; (b) examining the global associations between different heatwave types and ENSO events; and (c) identifying the influence of LWE exchange on modulating heatwave evolution across different climate zones.

## 2. Data

### 2.1. Air Temperature

The ERA5L (Muñoz-Sabater et al., 2021) is a state-of-the-art global reanalysis product that provides continuous meteorological variables in time and space by assimilating extensive ground observations and satellite data using a 4-dimensional variational assimilation system and a simplified extended Kalman filter system (Hersbach et al., 2020). Compared with previous reanalysis products, ERA5L has several advantages, including global coverage at an intermediate spatial resolution of  $0.1^{\circ}$ , decadal-long data records with enhanced accuracy (Sheridan et al., 2020; Zou et al., 2022), and improved temporal resolution (hourly), which allows for more precise detection of maximum and minimum daily temperatures ( $T_{\max}$  and  $T_{\min}$ ). In this study, we utilized hourly 2-m air temperatures from ERA5L to obtain daily  $T_{\max}$  and  $T_{\min}$  data, which were further used to estimate global DHW, NHW, and CHW from 1980 to 2022, respectively. In addition, we used air temperature data from three other independent data sets to validate the reliability of our estimates of interannual variation in different types of heatwaves, including the Climate Prediction Center (CPC) global unified temperature product (Pan et al., 2019), the Modern-Era Retrospective analysis for Research and Applications, Version 2 (MERRA2, Gelaro et al., 2017), and the second Japanese global atmospheric reanalysis project (JRA55, Kobayashi et al., 2015) (see Table 1).

### 2.2. Hydrometeorological Data and ENSO Index

In this study, we employed the Multivariate ENSO Index (MEI) version 2 from NOAA PSL to characterize ENSO variability (i.e., El Niño and La Niña episodes). The MEI index is derived from a combination of empirical orthogonal functions of several commonly observed variables (e.g., sea-level pressure, sea surface temperature, and outgoing longwave radiation) over the tropical Pacific region ( $30^{\circ}\text{S}$ – $30^{\circ}\text{N}$  and  $100^{\circ}\text{E}$ – $70^{\circ}\text{W}$ ) (Wolter & Timlin, 2011).

In addition, we used a set of global hydrometeorological variables to indicate the LWE exchanges, including: (a) terrestrial evapotranspiration (ET) and soil moisture ( $\theta$ ) from the Global Land Evaporation Amsterdam Model (GLEAM) version v3.7b, which is a widely-used ecohydrological product that assimilates remotely sensed surface soil moisture (Martens et al., 2017); (b) precipitation ( $P$ ) from the Multi-Source Weighted-Ensemble Precipitation (MSWEP) product, which merges gauge, satellite, and reanalysis data globally with demonstrated highest accuracy (Beck et al., 2019); (c) downward shortwave radiation (DSR) and downward longwave radiation (DLR) from the Multi-Source Weather (MSWX) product (Beck et al., 2022), where DSR includes both direct and diffuse solar radiation while the DLR represents the amount of thermal radiation emitted by the atmosphere and clouds that reaches the land surface; and (d) 10-m wind speed (WS) and relative humidity (RH) from MSWX, and vapor pressure deficit (VPD) calculated based on the MSWX-derived RH and air temperature.

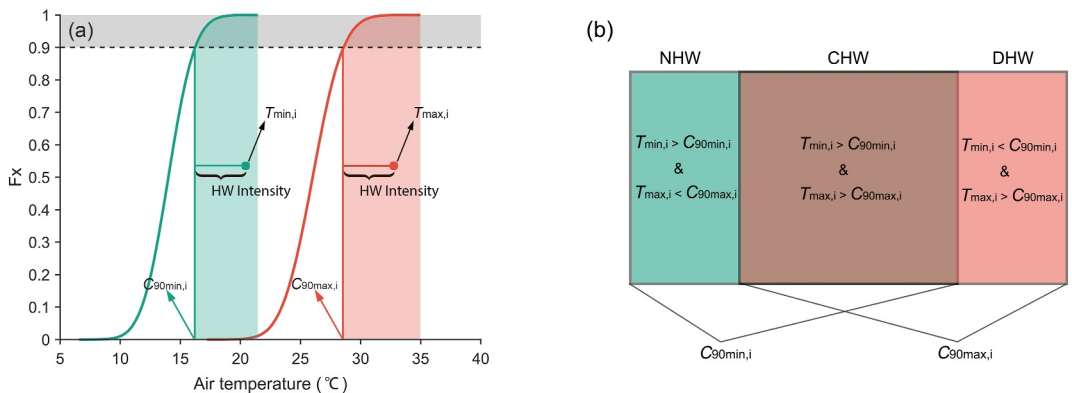


**Figure 1.** Schematic diagram of (a) determining the hot threshold of  $T_{\max}$  ( $C_{90\text{max}}$ ) and  $T_{\min}$  ( $C_{90\text{min}}$ ) using the eCDF ( $F_x$ ) for a specific day during the reference period; (b) the rule for identifying the DHW, NHW, and CHW.

It should be noted that ENSO significantly influences these LWE-related variables as it induces considerable deviations from normal climate conditions. A brief description of the ENSO impact on LWE-related factors can be found in Table S1 in Supporting Information S1.

### 3. Methods

#### 3.1. Heatwave Definition

The fundamental concept of heatwave relies on identifying high temperature anomalies in each grid cell when compared with their corresponding historical temperature ranges. Initially, a hot threshold is defined to ascertain if the temperature for a chosen grid on a specific date is sufficiently elevated. Typically, this hot threshold can be calculated at a particular percentile during the reference period (Figure 1a). In this context, the combined sets of temperatures ( $X_d$ ) for each grid on a given date, using a 31-day time window throughout the reference period (1981–2010), can be represented as follows (Russo et al., 2015):

$$X_d = \bigcup_{y=1981}^{2010} \bigcup_{d-15}^{d+15} T_{y,d} \quad (1)$$

where  $\bigcup$  denotes the union of sets,  $T$  is the time series of air temperatures for each grid,  $d$  is the given day, and  $y$  is the specific year. Consequently, the hot threshold for each grid at a given day can be determined by using the empirical cumulative distribution function (eCDF) at the 90th percentile of  $X_d$ :

Thus, the daily heatwave intensity (HWI<sub>daily</sub>) can be quantified as the surplus temperatures based on the hot threshold ( $C_{90}$ ) while also satisfying the temporal filter of three consecutive days (Equation 2):

$$\text{HWI}_{\text{daily}} = \max(T_a - C_{90}, 0)|_{\geq 3\text{day}} \quad (2)$$

where  $T_a$  is air temperature ( $^{\circ}\text{C}$ ). The hot thresholds for  $T_{\max}$  (i.e.,  $C_{90\text{max}}$ ) and  $T_{\min}$  (i.e.,  $C_{90\text{min}}$ ) were applied separately to identify the DHW, NHW, and CHW (Figure 1b). We repeated the above steps for all grids, allowing for global detection of different types of heatwaves. It should be noted that we utilized the hot threshold across all days of the year, rather than focusing the typical hot summer period. This approach helps avoid bias introduced by varying durations of seasonal differences across different regions globally. In addition, we evaluate annual heatwaves using two primary metrics: (a) the mean intensity of heatwaves (HWI), which indicates the temperature anomalies surpassed hot threshold throughout the study period; and (b) the frequency of heatwaves (HWF), calculated as the total number of heatwave days.

#### 3.2. LSTM and Global Sensitivity Analysis

In general, hot extreme events show clear temporal evolution, including onset, duration, and disappearance. LSTM model is well suited for modeling these events as their gating mechanisms enable them to capture long-

term dependencies and complex sequential patterns in meteorological factors, supporting accurate prediction and analysis of hot temperatures (Bonino et al., 2024; Khan & Maity, 2022; Liu et al., 2024). Hence, we used the LSTM model to establish a nonlinear neural network capable of capturing the temporal dynamics of their interactions to quantify the relationship between heatwave and LWE exchanges. Compared with traditional Recurrent Neural Networks (RNN), LSTM offers additional cell memory for state information storage and three gates (forget, input, and output) that regulate the retention of both long- and short-term memory (Hochreiter & Schmidhuber, 1997; Kratzert et al., 2018). In this study, our LSTM model was constructed using a configuration of 120 hidden layers, a single LSTM layer complemented by a fully connected layer, and a learning rate of 0.005. Key hyperparameters in LSTM were selected based on a grid search with five-fold cross-validation. We employed the Adam (adaptive moment estimation) optimizer as the solver for network training and used root mean square error (RMSE) instead of accuracy. The LSTM model was trained individually for each heatwave type and climate zone (based on the Köppen climate classification) to discern the relationships between the evolution of heatwaves and temporal sequences of seven environmental variables (Table 1). We specifically designed the model to predict heatwaves on day  $t$  based on the preceding environmental variables ( $t-10$ ), which enables the model to learn the dynamic relationship between LWE exchanges and heatwave evolution. The chosen  $t-10$  interval was identified to optimally reveal the relationship between LWE exchanges and heatwave evolution across the time-series, which can cover the average maximum life cycle of heatwave events (Thomas et al., 2020). All data samples were normalized via mean subtraction and standard deviation division for efficient learning (O. & Orth, 2021).

We employed the Sobol's method (Sobol, 2001) to further assess the relative importance of different variables influencing heatwaves within the well-trained LSTM models. Sobol indices provide a global sensitivity analysis approach designed to identify which input variables contribute most to the variance in a nonlinear system (Ali et al., 2024). By decomposing the output variance attributable to each variable or group of variables, Sobol analysis is well suited for nonlinear models and black-box interpretation (Fel et al., 2021). Recent studies have demonstrated that Sobol sensitivity analysis not only helps models eliminate unnecessary inputs but also provides reliable assessments of the relative importance of variables in deep learning networks (Y. Chen et al., 2021; Ren et al., 2023). Based on the Latin hypercube sampling (LHS) method (McKay, 1988), we set up a uniform perturbation space for each input variable with  $\pm 30\%$  over the time sequences. By applying Monte Carlo sampling, we can estimate the contribution of each variable to the output variance and calculate the corresponding Sobol indices, thereby quantitatively determining the importance of different variables in the LSTM model. Specifically, we performed Monte Carlo simulations with a sample size of 5,000, including a 500-iteration burn-in period. Notably, the final relative importance for each candidate variable was derived from the total-order of Sobol sensitivity indices. More details on the Sobol's method can be found in Supporting Information S1.

## 4. Results

### 4.1. Spatio-Temporal Patterns of DHW, NHW, and CHW

We observed large spatial differences in mean annual heatwave frequency (HWF) and intensity (HWI) over the past 43 years (1980–2022), regardless of DHW (Figures 2a and 2b), NHW (Figures 2c and 2d), and CHW (Figures 2e and 2f). While DHW and NHW display similar spatial patterns, DHW exhibits higher absolute values for mean annual frequency and intensity compared with NHW. Tropical regions generally experience greater mean annual frequency and intensity than extra-tropical regions for both DHW and NHW, whereas CHW demonstrates substantially higher frequency and intensity in high-latitude regions, such as the Arctic and Antarctica.

These similarities and differences are also reflected across the climate zone. The mean annual frequency of DHW was highest in the tropical zone ( $7.15 \pm 2.8$  days year $^{-1}$ ), followed by temperate ( $5.67 \pm 1.5$  days year $^{-1}$ ), dryland ( $4.8 \pm 1.64$  days year $^{-1}$ ), continental ( $1.89 \pm 0.48$  days year $^{-1}$ ), and polar regions ( $0.62 \pm 0.14$  days year $^{-1}$ ). The mean annual frequency of NHW follows the same order, but with an average of 0.34 days less than those of DHW. The mean annual frequency of CHW differs from the other two, with the highest value in polar regions ( $13.55 \pm 3.51$  days year $^{-1}$ ), followed by continental climate ( $8.26 \pm 2.85$  days year $^{-1}$ ) while the tropics have the lowest value ( $4.83 \pm 5.31$  days year $^{-1}$ ). The relative order of mean annual intensity is overall comparable between DHW and NHW (Figures 2b and 2d), with the highest value of  $0.82 \pm 0.13^\circ\text{C year}^{-1}$  in temperate zone for DHW

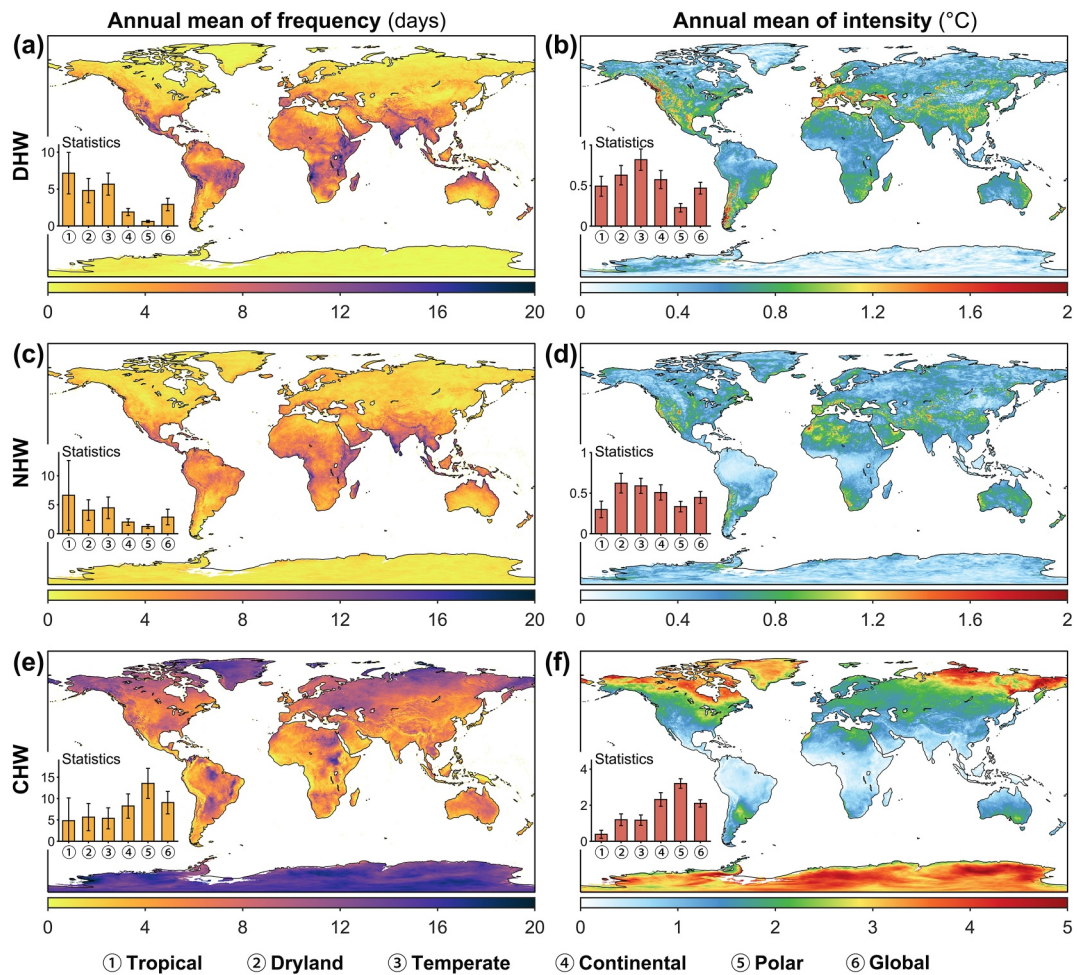


**Figure 2.** Climatological mean annual heatwave frequency (HWF) and intensity (HWI) from 1980 to 2022. The DHW, NHW, and CHW are indicated in each row from top to bottom. The left (right) column denotes the heatwave frequency (intensity). Insets in each panel display the mean annual frequency and intensity of heatwaves for five major climate zones (see Figure S1 in Supporting Information S1).

and  $0.62 \pm 0.12^\circ\text{C year}^{-1}$  in dryland for NHW. The relative order of mean annual intensity of CHW differs from the other two, with the mean annual intensity highest at  $3.2 \pm 0.27^\circ\text{C year}^{-1}$  in the polar regions.

Over the past decades, all three types of heatwaves have experienced increasing occurrence and severity, as indicated by the predominance of positive trends of annual frequency and intensity (Figure 3). DHW and NHW exhibit remarkably similar patterns, with more pronounced increases in frequency in the tropics and smaller increase trends in extra-tropical regions (Figures 3a and 3c). While CHW shows a stronger increasing trend in frequency within the tropics, they also display significant positive trends in extra-tropical regions (Figure 3e). However, the patterns of intensity trend differ from those of frequency trends. The highest increases in heatwave intensity are observed in the mid- and high latitudes of the Northern Hemisphere, particularly in Eurasia, rather than in the tropical zone (Figure 3f).

The annual trends of frequency and intensity also display significant dependency on climate zones (bar plots in Figure 3). The trends of annual frequency are overall similar across all three heatwave types, with the highest values in the tropics and the lowest in polar regions. Nonetheless, the global average trend of annual frequency is much larger in CHW ( $0.15 \text{ days year}^{-1}$ ) than in DHW ( $0.06 \text{ days year}^{-1}$ ) and NHW ( $0.08 \text{ days year}^{-1}$ ). The annual trends of intensity for climate zones differ from those of frequency, with higher values in dryland and temperate zones, and the lowest in polar regions, consistently across all three heatwave types. Meanwhile, the absolute values of annual trends in intensity almost double in CHW compared with the other two types, with a

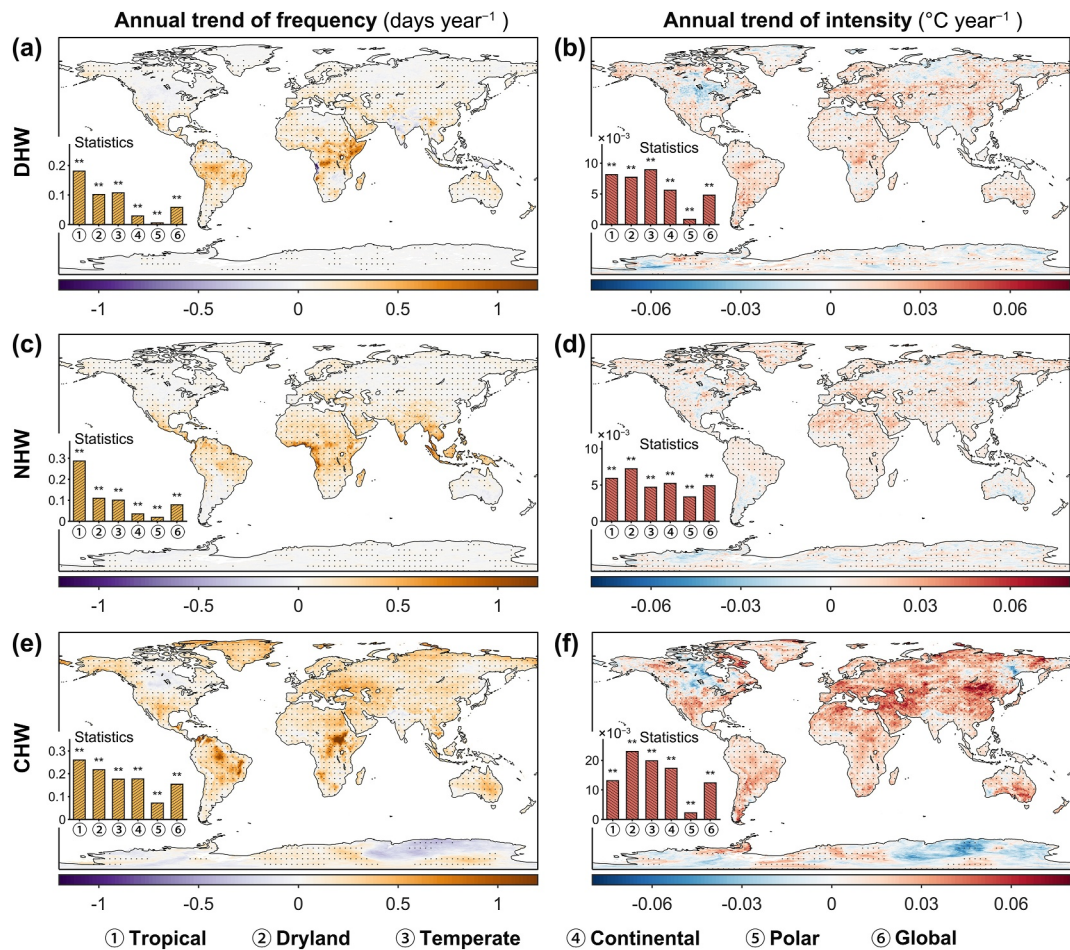


**Figure 3.** Spatial patterns of the trend in annual frequency (left column) and intensity (right column) for DHW, NHW, and CHW from 1980 to 2022. The dotted points within the grid cells indicate statistically significant trends ( $p < 0.01$ ) based on the Mann-Kendall (MK) trend test. The inset in each panel shows the trend magnitudes for the five major climate zones and global average, with the asterisks (\*\*) denote their trend values that are statistically significant according to the MK test.

global average trend of intensity of  $12.38 \times 10^{-3} \text{ }^{\circ}\text{C year}^{-1}$  in contrast to  $4.81 \times 10^{-3} \text{ }^{\circ}\text{C year}^{-1}$  in DHW and  $4.89 \times 10^{-3} \text{ }^{\circ}\text{C year}^{-1}$  in NHW.

#### 4.2. Associations Between ENSO and Different Types of Heatwaves

As shown in Figure 4, global annual frequency and intensity of heatwaves, derived from multiple data sources, both show significant increasing trends over the past 43 years, consistently across all three heatwave types. The annual trends of global mean frequency and intensity are overall comparable between DHW and NHW, but are 1/3 to 1/2 smaller than those in CHW. When overlapped with ENSO time series, we observed that most of positive spikes in global mean frequency and intensity correspond to strong El Niño episodes while most negative spikes correspond to strong La Niña episodes. These associations are consistent across three heatwave types.

We next analyzed the difference in heatwave frequency ( $\Delta\text{HWF}$ ) and intensity ( $\Delta\text{HWI}$ ) between El Niño and La Niña years. Our results indicate that heatwave characteristics differ significantly between these two ENSO phases, with the magnitude and direction of these effects varying considerably across climate zones (Figure 5). Specifically, the spatial patterns of  $\Delta\text{HWF}$  and  $\Delta\text{HWI}$  for the same type of heatwave are generally consistent under ENSO episodes; however, the proportion of strongly affected areas differs markedly among climate zones (bar plot in Figure 5). For example, the frequency of DHW in tropical regions is particularly sensitive to ENSO oscillations, with the fractions of strongly positive and negative areas reaching 34% and 24%, respectively (Figure 5a). In contrast, the impact of ENSO on HWI is more pronounced in continental and polar zones than in

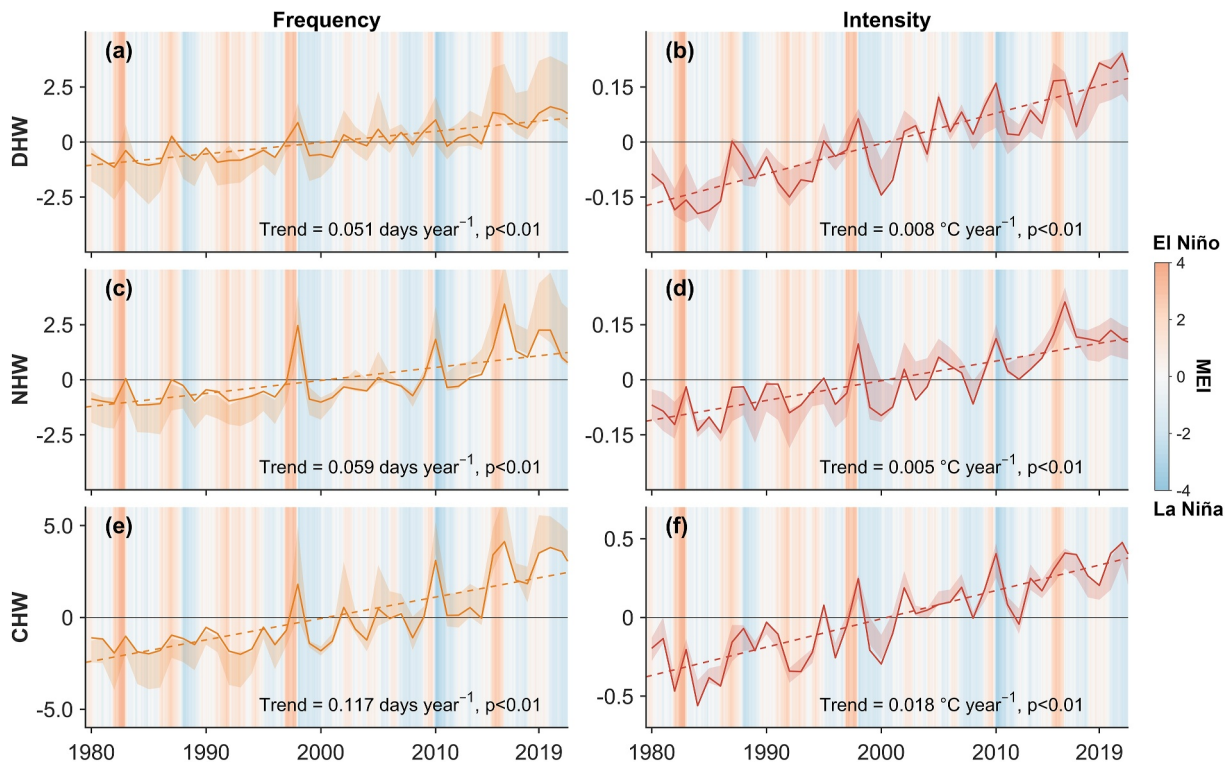


**Figure 4.** Annual anomalies in the frequency and intensity of global daytime, nighttime, and compound heatwaves from 1980 to 2022. The shading areas represent the  $\pm 1$  standard deviation of the anomalies, calculated from four air temperature data sets: ERA5L, CPC, MERRA2, and JRA55. The dashed lines indicate the least-squares-fitted linear trend for the combined data sets, with corresponding  $p$ -values derived from the Mann-Kendall trend test. Vertical color shading indicates ENSO transitions, represented by the Multivariate ENSO Index (MEI), where red and blue shades denote positive (El Niño) and negative (La Niña) phases, respectively, and the darker shades indicate stronger ENSO intensity.

the tropics (Figure 5b). Similar spatial patterns are observed for NHW and CHW (Figures 5c–5f). Notably, for CHW, most high-latitudes in the Northern Hemisphere with continental climates exhibit negative  $\Delta$ HWF and  $\Delta$ HWI values, with up to 60% of these areas showing negative trends, suggesting that CHW is more likely during La Niña years in regions such as the Caucasus, Siberia, and northeastern Canada. Additionally, it is noteworthy that ENSO-related heatwave frequency in China exhibits a distinct north-south difference, with northern China more prone to heatwaves during El Niño years while southern China experiencing a higher likelihood of extreme heat during La Niña years.

Further analysis demonstrates that the annual anomalies during ENSO episodes for different types of heatwaves vary largely across multiple climate zones (Figure 6). Regarding frequency, all heatwave types in the tropics show a distinct pattern during ENSO events (Figures 6a and 6c), with strong positive anomalies in El Niño years (e.g., +5 days on average for NHW and CHW) and strong negative anomalies in La Niña years (e.g., -2 days on average for NHW and CHW). Similar patterns are observed in dryland and temperate regions, although the degree of variance in heatwave frequency is notably lower than in the tropics. In continental and polar climate zones, where DHW and NHW heatwaves are infrequent, the magnitude of frequency anomalies during ENSO periods becomes negligible, ranging from  $\pm 0.1$  days on average. However, statistics for CHW reveal that in continental zones, there are more CHW on average (+0.5 days) during La Niña episodes compared with El Niño episodes (-0.4 days). Furthermore, in polar regions, the frequency of CHW does not show an opposite phenomenon during ENSO, with both showing an averaged negative anomaly of -1 and -2 days per year, respectively (Figure 6e).

Similarly, heatwave intensity in tropical regions exhibits clear positive anomalies during El Niño years and generally negative values during La Niña years. This contrast is particularly pronounced for NHW and CHW, with no overlaps of  $\pm 1$  standard deviation of heatwave intensity between El Niño and La Niña episodes (Figures 6d and 6f). In dryland and temperate zones, heatwave intensity ranges are comparable throughout ENSO, with more severe heatwaves during El Niño than La Niña episodes, except for DHW in temperate regions

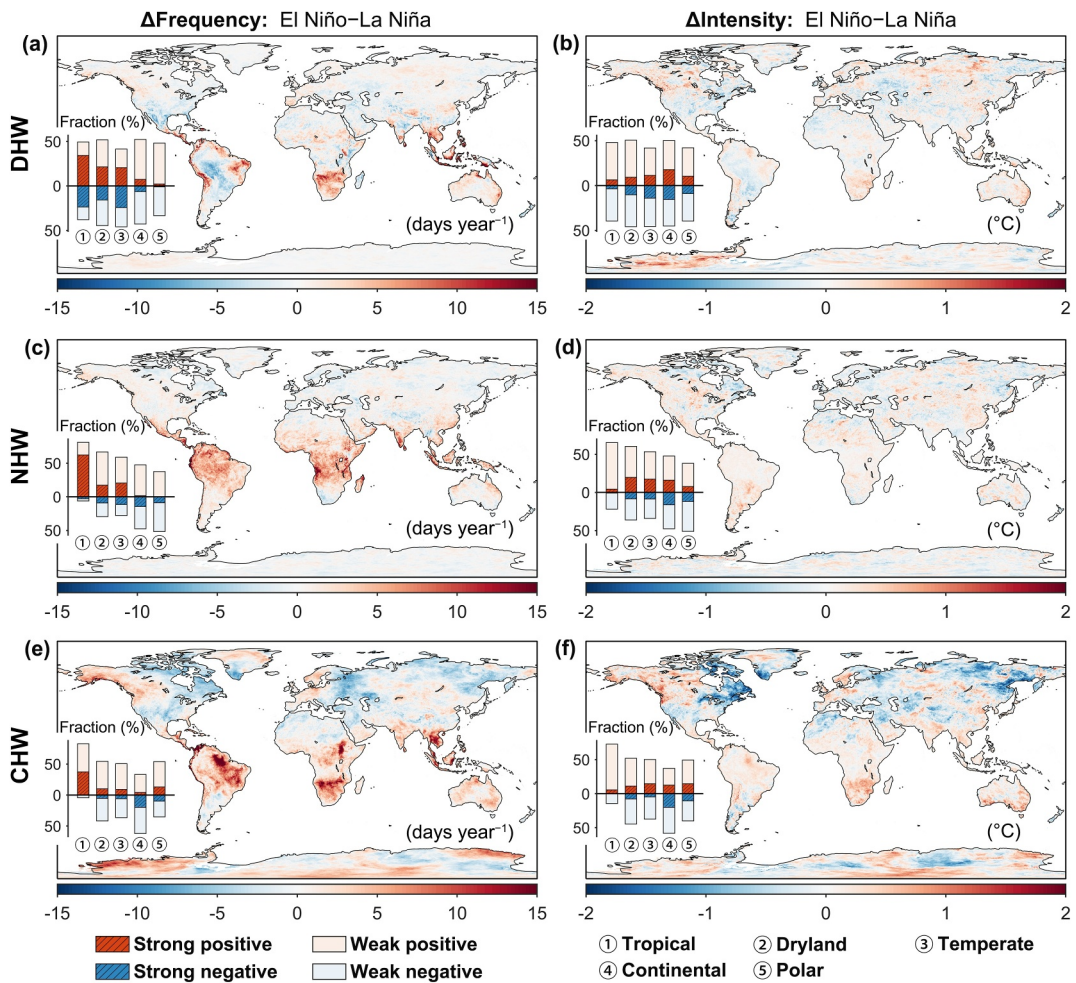


**Figure 5.** Spatial differences in the frequency and intensity of daytime, nighttime, and compound heatwaves between El Niño and La Niña years. In each subpanel, the bar plot shows the proportion of areas with positive (more frequent/severe heatwaves during El Niño) and negative (more frequent/severe heatwaves during La Niña) anomalies across different climate zones. The dark-colored portions of each bar indicate the fraction of strongly positive or negative areas, defined as those exceeding the 75th percentile of positive or negative variations based on their cumulative density functions.

(Figure 6b). Moreover, different types of heatwaves demonstrate varying intensities in response to ENSO episodes in continental and polar zones. For instance, ENSO does not appear to have a substantial impact on DHW, whereas in polar regions, DHW intensities are greater during El Niño than during La Niña. The interannual variability of CHW in continental and polar regions is also considerably greater than in other climate zones. Nonetheless, on a global scale, DHW and NHW are more likely to occur with stronger intensity during El Niño episodes, whereas they are generally less frequent and of weaker intensity during La Niña episodes. Regardless, we observed that CHW occurs more frequent during El Niño than during La Niña, but their corresponding intensities are the opposite.

#### 4.3. The Association of Heatwaves With LWE Exchanges

To explore whether and how LWE exchanges affect the temporal evolution of heatwaves, we trained LSTM models for each of the five major climate zones using multiple hydrometeorological variables. The coefficient of determination ( $R^2$ ) is used as an accuracy metric to evaluate the performance of LSTM training. It quantifies the proportion of variance in the dependent variable that is explained by the model (see Supporting Information S1). Our trained LSTM models perform well in capturing the time evolution of heatwaves, with an average  $R^2$  across all five climate zones of 0.83 for heatwave frequency and 0.79 for heatwave intensity (Table 2). Among all five climate zones, the LSTM model displays the highest accuracy in tropics ( $R^2 = 0.92$  for frequency and 0.88 for

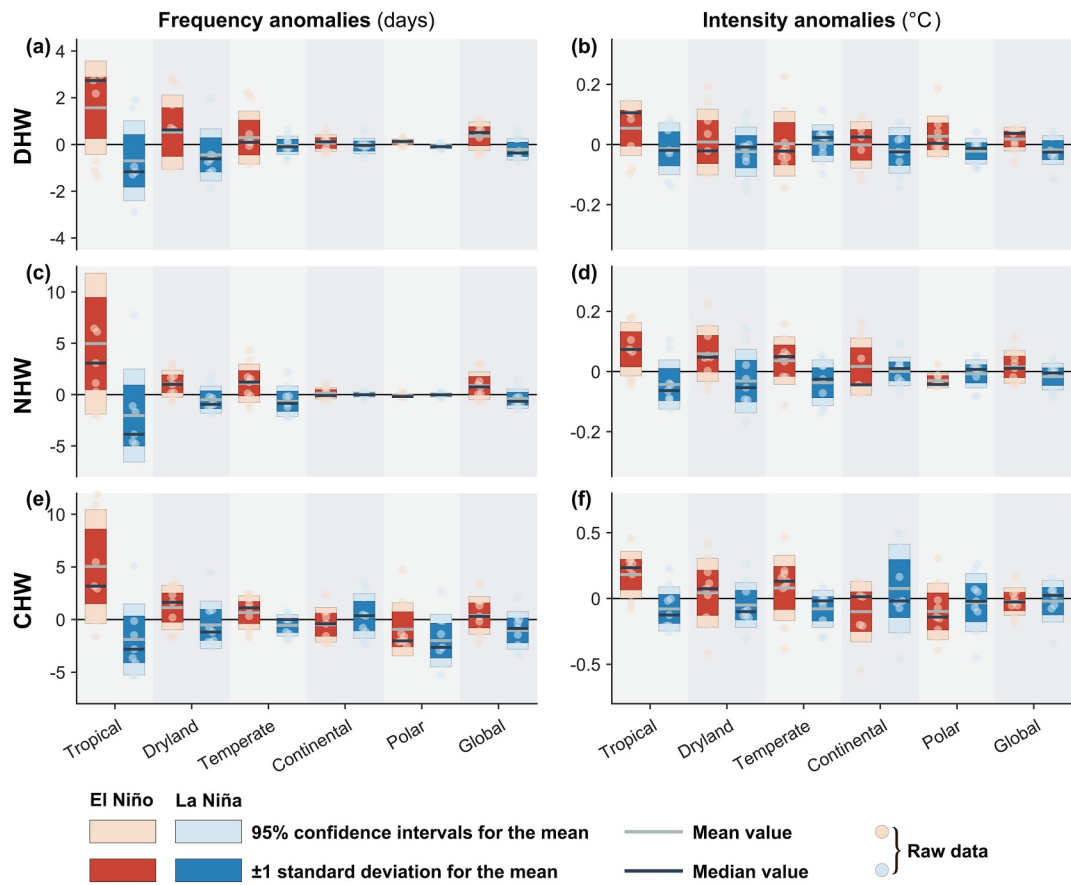


**Figure 6.** Comparison of annual anomalies in heatwave frequency and intensity of DHW, NHW, and CHW for the selected El Niño (red) and La Niña (blue) years across major climate zones. Each light-colored box represents the 95% confidence intervals for the mean value (gray line) while the dark-colored box represents the range of  $\pm$  standard deviation for the mean value. The black line in each box denotes the median value of selected data.

**Table 2**

*The Determination Coefficient ( $R^2$ ) of the Trained LSTM Networks for the Test Samples and Overall Samples in Different Heatwave Types Across Multiple Climate Zones*

	Tropical		Dryland		Temperate		Continental		Polar		Global	
	$R^2_{\text{test}}$	$R^2_{\text{all}}$										
<b>Frequency</b>												
DHW	0.85	0.93	0.76	0.90	0.62	0.86	0.69	0.84	0.62	0.88	0.68	0.87
NHW	0.95	0.98	0.79	0.92	0.67	0.87	0.63	0.81	0.68	0.86	0.81	0.91
CHW	0.96	0.98	0.83	0.93	0.73	0.88	0.71	0.86	0.84	0.94	0.80	0.91
Averaged	0.92	0.96	0.79	0.92	0.67	0.87	0.68	0.84	0.71	0.89	0.76	0.90
<b>Intensity</b>												
DHW	0.81	0.92	0.72	0.88	0.58	0.84	0.66	0.82	0.53	0.85	0.62	0.85
NHW	0.91	0.96	0.73	0.90	0.56	0.78	0.55	0.77	0.54	0.84	0.68	0.85
CHW	0.93	0.97	0.80	0.91	0.68	0.88	0.65	0.86	0.82	0.93	0.76	0.91
Averaged	0.88	0.95	0.75	0.90	0.61	0.83	0.62	0.82	0.63	0.87	0.69	0.87

*Note.* The  $R^2_{\text{test}}$  denotes the accuracy based on the independent test samples while the  $R^2_{\text{all}}$  represents the accuracy evaluation based on the overall samples. Comparing  $R^2_{\text{test}}$  and  $R^2_{\text{all}}$  helps assess model generalization, data distribution consistency, and detect potential data leakage.

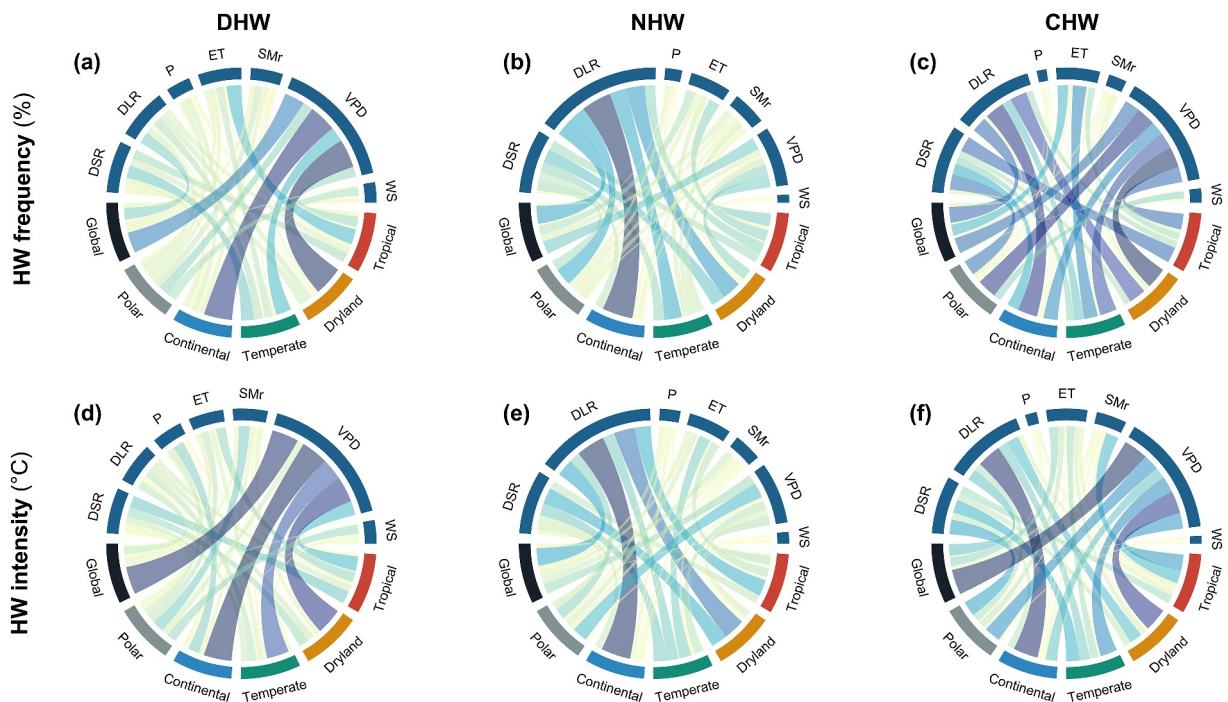


**Figure 7.** Chord diagram to illustrate the linkages of local water-energy factors to the heatwave variations across climate zones. Each circle represents the specific frequency or intensity of daytime, nighttime, and compound heatwaves, respectively. In particular, the top half of each circle shaded in dark blue indicates the water-energy-related variables, which include downward shortwave radiation (DSR), downward longwave radiation (DLR), precipitation (P), evapotranspiration (ET), soil moisture (SM), vapor pressure deficit (VPD), and wind speed (WS). The bottom half of each circle denotes the global and different climate zones.

intensity based on the independent test samples within the same climate zone), followed by dryland ( $R^2 = 0.79$  for frequency and 0.75 for intensity), and the lowest in temperate, continental, and polar climate zones, but still achieving an  $R^2$  higher than 0.61.

Based on the accuracy of the trained LSTM model in capturing the temporal evolution of heatwaves, we used Sobol's total-order sensitivity indices (see Section 3) to assess the relationships between key environmental factors and two heatwave metrics (i.e., frequency and intensity) across different climate zones and heatwave types (Figure 7). Overall, we observed significant variations in the links between local hydrometeorological conditions and heatwave metrics across different heatwave types and climate zones. Considering DHW as an example, we observe that in dryland, temperate, continental, and global (all climate zones combined) regions, VPD exhibits a strong association with both the frequency and intensity of heatwaves (Figures 7a and 7d). In contrast, within the tropics, ET and DSR are found to be the most relevant factors to heatwave frequency while VPD, ET, and DSR are most strongly linked to heatwave intensity. While VPD consistently emerges as the environmental variable most closely associated with DHW frequency and intensity (Figures 7a and 7d), DLR is most strongly linked to NHW frequency and intensity (Figures 7b and 7e), especially for dryland and continental zones. In tropical regions, VPD, ET, DLR, and DSR all display notable associations with NHW frequency while DLR, DSR and ET are most relevant to NHW intensity. Finally, the relationships between environmental factors and CHW are more complex (Figures 7c and 7f), but generally reflect a combination of the dominant associations identified for both DHW and NHW.

In addition, we performed experimental analyses using the trained LSTM model by controlling the dynamic variations of soil moisture (SM) and evapotranspiration (ET) associated with land-atmosphere interactions, in order to quantify their impacts on local heatwaves variations. The difference in the coefficient of determination ( $\Delta R^2$ ) is used to evaluate the results of the control experiments. Specifically, a lower  $\Delta R^2$  indicates that the time-series dynamic evolution of evapotranspiration and soil moisture plays a more significant role in heatwave prediction. As shown in Figure 8, the difference in determination coefficient ( $\Delta R^2$ ) of both heatwave frequency and intensity in dryland and temperate zones is reduced the most (ranging from -0.15 to -0.25 across different heatwave types) compared with other climate zones. This indicates that the temporal evolution of heatwaves in

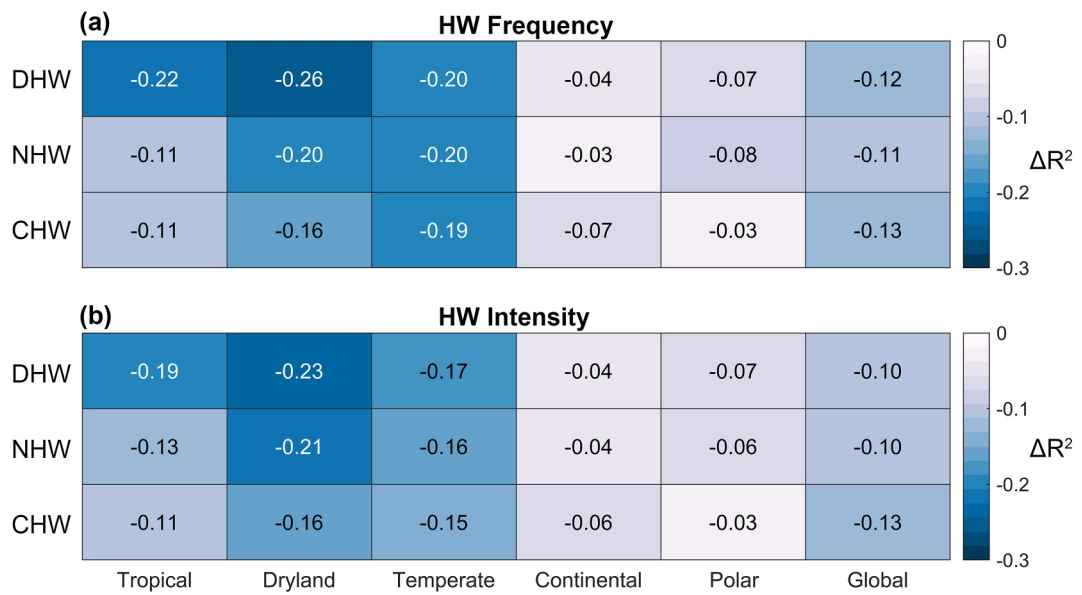


**Figure 8.** Differential performance in predicting heatwaves for different types of heatwaves across various climate zones by controlling the dynamic variations of evapotranspiration and soil moisture.

dryland and temperate zones depends more on the interactions with LWE exchange in terms of changes in SM and ET. In contrast, negligible impacts with a mean  $\Delta R^2$  of  $-0.05$  and  $-0.06$  are observed for continental and polar climate zones, respectively, indicating that the heatwave evolution is rarely influenced by the dynamic changes of ET and SM in these climate zones. In addition, we observed that DHW in tropical regions display higher sensitivity responses to ET and SM (i.e.,  $-0.22$  for heatwave frequency and  $-0.19$  for heatwave intensity), aligning with the results in Figure 7a. When considering these findings on a global scale, we also noticed that CHW demonstrates slightly higher sensitivity responses to SM and ET compared to the other two heatwave types.

## 5. Discussion

Heatwaves have become more frequent and intense in recent decades (Meehl & Tebaldi, 2004; Perkins-Kirkpatrick & Lewis, 2020; Wouters et al., 2022). Our results reveal a significant and persistent upward trend in both frequency and intensity of global heatwaves from 1980 to 2022. Notably, CHW has exhibited a two- to three-fold increase in both frequency and intensity compared with DHW and NHW. Thus unlike DHW and NHW, which often exhibit distinct environmental backgrounds (Luo et al., 2022), the increase of CHW with complex mechanisms poses heightened risks for both natural ecosystems and human societies (Ma, Yuan, Wu, & Zeng, 2022).

The spatial patterns of annual mean values and trends for different types of heatwaves exhibit considerable differences across climate zones. Our results indicate that, over the past 43 years, polar and cold regions have experienced more frequent and severe CHW (Figure 2). This can be attributed to the greater temperature variability in high-latitude areas, which stems from factors such as pronounced fluctuations in solar radiation, higher surface albedo, and lower heat capacity due to the sparse vegetation and limited moisture compared to the tropics. While certain tropical regions (e.g., the Amazon) display higher increases in heatwave frequency (Figure 3), these trends are mainly influenced by the occurrence of severe heatwaves during a few exceptional years (e.g., 1998, 2010, and 2015; see Figure S2 in Supporting Information S1). When considering both frequency and intensity of heatwaves, as indicated by the annual cumulative intensity of CHW, high-latitude regions still exhibit the highest increasing trend, especially after the year 2000 (Figure S2 in Supporting Information S1). This trend can be linked to polar amplification of warming (Cai, 2005; Gillett et al., 2008; Taylor et al., 2013). Abnormally high temperatures accelerate the melting of ice sheets and glaciers, especially in alpine mountains in cold regions, driving recent hazards such as ice avalanches (Shugar et al., 2021; Y. Zhou et al., 2021). However, the most rapid increases in heatwave intensity have occurred in non-polar regions, particularly in dryland and temperate zones, suggesting that these regions have experienced progressively stronger heatwaves over the last four decades (Figure 3). Recent studies suggest that changes in local environmental conditions (e.g., land use and land cover,

greenhouse gas emissions) resulting from human activities are likely the main causes to intensifying heatwaves (Christidis et al., 2015; Liang et al., 2022; Stott et al., 2004).

Our research reveals significant spatial variations in the impacts of ENSO on different types of heatwaves. These ENSO effects are particularly pronounced in tropical regions, where both the frequency and intensity of heatwaves are significantly higher during El Niño years compared with La Niña years (Figure 6). The underlying mechanism involves ENSO-driven sea surface temperature (SST) anomalies, which fundamentally alter large-scale atmospheric circulation patterns. During El Niño episodes, the weakening of the Walker circulation and shifts in the position and intensity of the jet streams redistribute convection, precipitation, and heat transport (McPhaden et al., 2006). These changes in atmospheric and surface conditions lead to temperature anomalies and create a favorable environment for hot extremes. Specifically, El Niño can promote the formation of blocking highs that suppress cloud development and precipitation, resulting in prolonged periods of intense solar heating for heatwave formation. Furthermore, reduced rainfall during El Niño can lead to drought, depleting soil moisture and weakening surface evaporative cooling. This drying effect further reinforce warming, creating self-amplifying heating cycles and increasing heatwave risk (Miralles et al., 2019).

Previous studies have identified extreme hot temperatures in tropical regions during El Niño episodes, particularly in the Amazon and Southeast Asia (Bennett et al., 2023; Thirumalai et al., 2017). For example, during El Niño, anomalous sinking air replaces the usual rising branches over the Amazon and Southeast Asia (Power & Smith, 2007), leading to adiabatic compression heating with reduced cloud cover, which allow for greater absorption of solar radiation at the land surface (Asner et al., 2000; Luther et al., 1983). Additionally, the weakened trade winds along the tropical Pacific during El Niño further enhance heat accumulation in these regions (Kang et al., 2018; Kautz et al., 2022). In contrast, central Africa experiences only minimal temperature increases during El Niño (Figure S3 in Supporting Information S1), largely due to prevailing upward airflow that limits surface warming. Nevertheless, the advection of external heat sources can still contribute to local temperature anomalies, highlighting the complex trade-off from multiple factors.

Compared with the impact of ENSO on heatwaves, which leads to differences across various climate zones, local land-atmosphere interactions are more strongly associated with the characteristics of different heatwave types. The LWE exchange is severely affected during hot extremes, and enhanced land-atmosphere interactions play a crucial role in the development and propagation of heatwaves (Miralles et al., 2019; Wouters et al., 2022). Utilizing the LSTM model, we identified that VPD exhibits the strongest association with DHW (Figures 7a and 7d), which typically occur under hot and dry conditions under clear skies (Luo et al., 2022). In these low humidity environments, VPD fluctuations are more pronounced and closely correlated with high temperatures (Lansu et al., 2020). It is important to note that while VPD dynamics do not directly cause the occurrence of heatwaves, they play a significant role in amplifying and sustaining heatwave intensity and duration through land-atmosphere feedbacks (Miralles et al., 2014).

In contrast, for NHW, DLR has a more prominent association than other variables and is the dominant factor linked to heatwave variations (Figures 7b and 7e). Typically, DLR is intensified by absorbing more surface outgoing longwave radiation due to an enhanced greenhouse effect from increased water vapor flux (R. Chen & Lu, 2014; Stephens et al., 2012) and reemitting stronger longwave radiation due to moisture advection leading to cloud generation (Naud et al., 2013; Sato & Simmonds, 2021). Consequently, NHW is primarily characterized by hot and humid conditions (Hong et al., 2018), posing a greater threat to humanity (Wouters et al., 2022). Recent research by Wu et al. (2023) further examined changes in moisture transport and distribution associated with different heatwave types. Their findings indicate that DHW are linked to positive anomalies in moisture divergence, leading to warmer and drier conditions with reduced humidity and cloud cover. Conversely, NHW exhibits a distinct pattern of moisture transport from ocean to land, resulting in elevated humidity and increased cloud cover. Comparatively, as reflected by the more balanced relative importance of the radiation term and VPD (Figure 7c), CHW exhibits a more complex relationship to LWE changes, combining independent characteristics of both DHW and NHW.

In addition, distinct local environmental conditions along with land-atmosphere feedbacks, can substantially influence the temporal variation of air temperatures, and hence the severity of heatwaves (Miralles et al., 2014; Seneviratne et al., 2010). To specifically assess the role of land feedbacks, we conducted LSTM experiments in which evapotranspiration and soil moisture were held constant over time, thereby isolating the effect of their

temporal variation. Under these conditions, heatwaves in dryland and temperate regions are most influenced, whereas continental and polar regions are merely affected (Figure 8). In water-limited regions, evapotranspiration is highly dependent on soil moisture (Denissen et al., 2022; Zhang et al., 2022), where land-atmosphere interactions are largely governed by water availability (Huang et al., 2017). As a result, the dynamics of land-atmosphere feedbacks, particularly under condition of high atmospheric water demand, become especially important for surface energy partitioning in these areas (Gerken et al., 2019; Huang et al., 2017; Schumacher et al., 2020). Temperate zones, which serve as significant transitional regions, also display strong coupling between soil moisture and evapotranspiration, which exerts a profound influence on surface temperature (Sen-evilatne et al., 2006, 2010).

By contrast, the effect of land feedback on heatwaves in continental and polar regions is relatively minor. This can be attributed to lower climatological temperatures, according to the Clausius-Clapeyron relation, resulting in limited water exchange capacity. In tropical regions, high temperatures and abundant water supply maintain a high vapor capacity. The available radiation, rather than land feedbacks, primarily controls sensible heat allocation, and land-atmosphere interactions are often modulated by shallow clouds (Gentine et al., 2019). Therefore, the dynamics of tropical evapotranspiration and soil moisture have a relatively minor effect on NHW and CHW under hot-wet conditions, but play a considerable role in DHW accompanied by hot-dry weather.

## 6. Conclusion

In this study, we assessed the global patterns of daytime, nighttime, and compound heatwaves over the past 43 years using air temperature data from ERA5L. Our results reveal distinct spatiotemporal patterns among the three heatwave types, with DHW and NHW being more prevalent in low and mid-latitudes, and CHW showing higher frequency and severity in high-latitude regions. An increasing trend in the occurrence of all three heatwave types is identified, and dryland and temperate regions show the most pronounced intensity, especially in the case of CHW. A strong connection exists between heatwaves and ENSO, with higher frequencies and intensities during El Niño years, particularly in tropical regions. This association is attributed to the ENSO-induced Walker circulation anomalies. Using LSTM, we established time-dependent relationships between local water-energy exchanges and various heatwave types across major climate zones. The results reveal that VPD dynamics play a crucial role in DHW evolution while downward longwave radiation is most significantly linked to NHW. However, the influencing factors affecting CHW show a more complex and non-dominant pattern. By controlling LWE exchanges on heatwave evolution through evapotranspiration and soil moisture dynamics, we found that dryland and temperate regions are more susceptible to these influences. Overall, our results highlight the importance of land feedbacks in heatwave evolution, and will enhance our understanding of heatwave patterns and their implications on a global scale, ultimately aiding in the development of effective strategies for heatwave mitigation.

## Conflict of Interest

The authors declare no conflicts of interest relevant to this study.

## Data Availability Statement

The air temperature data used for calculating heatwaves were obtained from ERA5-Land (Muñoz-Sabater et al., 2021), MERRA-2 (Gelaro et al., 2017), CPC (Pan et al., 2019), and JRA-55 (Kobayashi et al., 2015). Evapotranspiration (ET) and soil moisture data were sourced from GLEAM (Martens et al., 2017). Downward shortwave radiation (DSR), downward longwave radiation (DLR), wind speed (WS), and relative humidity (RH) were obtained from the Multi-Source Weather (MSWX) product (Beck et al., 2022). Precipitation data were taken from the Multi-Source Weighted-Ensemble Precipitation (MSWEP) product (Beck et al., 2019). The heatwave data set generated in this study is available from the National Tibetan Plateau Data Center (Zhang, 2025).

## References

- Alexander, M. A., Bladé, I., Newman, M., Lanzante, J. R., Lau, N.-C., & Scott, J. D. (2002). The atmospheric bridge: The influence of ENSO teleconnections on air-sea interaction over the global oceans. *Journal of Climate*, 15(16), 2205–2231. [https://doi.org/10.1175/1520-0442\(2002\)015<2205:TABTIO>2.0.CO;2](https://doi.org/10.1175/1520-0442(2002)015<2205:TABTIO>2.0.CO;2)
- Ali, M., Sarwar, T., Mubarak, N. M., Karri, R. R., Ghalib, L., Bibi, A., & Mazari, S. A. (2024). Prediction of CO<sub>2</sub> solubility in ionic liquids for CO<sub>2</sub> capture using deep learning models. *Scientific Reports*, 14(1), 14730. <https://doi.org/10.1038/s41598-024-65499-y>

## Acknowledgments

The work was primarily supported by National Natural Science Foundation of China (31922090), National Key Research and Development Program of China (No. 2018YFA0605601), Hong Kong Research Grant Council General Research Fund (17316622 and 17305321). Jin Wu was also supported by the HKU Seed Funding for Strategic Interdisciplinary Research Scheme, the Hung Ying Physical Science Research Fund (2021-22), and the Innovation and Technology Fund (funding support to State Key Laboratory of Agrobiotechnology).

- Asner, G. P., Townsend, A. R., & Braswell, B. H. (2000). Satellite observation of El Niño effects on Amazon Forest phenology and productivity. *Geophysical Research Letters*, 27(7), 981–984. <https://doi.org/10.1029/1999GL011113>
- Baldwin, J. W., Dassy, J. B., Vecchi, G. A., & Oppenheimer, M. (2019). Temporally compound heat wave events and global warming: An emerging hazard. *Earth's Future*, 7(4), 411–427. <https://doi.org/10.1029/2018EF000989>
- Beck, H. E., Wood, E. F., Pan, M., Fisher, C. K., Miralles, D. G., van Dijk, A. I. J. M., et al. (2019). MSWEP V2 global 3-hourly 0.1° precipitation: Methodology and quantitative assessment. *Bulletin of the American Meteorological Society*, 100(3), 473–500. <https://doi.org/10.1175/BAMS-D-17-0138.1>
- Beck, H. E., van Dijk, A. I. J. M., Larraondo, P. R., McVicar, T. R., Pan, M., Dutra, E., & Miralles, D. G. (2022). MSWX: Global 3-hourly 0.1° bias-corrected meteorological data including near-real-time updates and forecast ensembles. *Bulletin of the American Meteorological Society*, 103(3), E710–E732. <https://doi.org/10.1175/BAMS-D-21-0145.1>
- Bennett, A. C., Rodrigues de Sousa, T., Monteagudo-Mendoza, A., Esquivel-Muelbert, A., Morandi, P. S., Coelho de Souza, F., et al. (2023). Sensitivity of South American tropical forests to an extreme climate anomaly. *Nature Climate Change*, 13(9), 967–974. <https://doi.org/10.1038/s41558-023-01776-4>
- Bonino, G., Galimberti, G., Masina, S., McAdam, R., & Clementi, E. (2024). Machine learning methods to predict sea surface temperature and marine heatwave occurrence: A case study of the Mediterranean Sea. *Ocean Science*, 20(2), 417–432. <https://doi.org/10.5194/os-20-417-2024>
- Bowd, E. J., Banks, S. C., Strong, C. L., & Lindenmayer, D. B. (2019). Long-term impacts of wildfire and logging on forest soils. *Nature Geoscience*, 12(2), 113–118. <https://doi.org/10.1038/s41561-018-0294-2>
- Brás, T. A., Seixas, J., Carvalhais, N., & Jägermeyr, J. (2021). Severity of drought and heatwave crop losses tripled over the last five decades in Europe. *Environmental Research Letters*, 16(6), 065012. <https://doi.org/10.1088/1748-9326/abf004>
- Cai, M. (2005). Dynamical amplification of polar warming. *Geophysical Research Letters*, 32(22). <https://doi.org/10.1029/2005GL024481>
- Chen, R., & Lu, R. (2014). Dry tropical nights and wet extreme heat in Beijing: Atypical configurations between high temperature and humidity. *Monthly Weather Review*, 142(5), 1792–1802. <https://doi.org/10.1175/MWR-D-13-0028.1>
- Chen, Y., Liu, G., Huang, X., Chen, K., Hou, J., & Zhou, J. (2021). Development of a surrogate method of groundwater modeling using gated recurrent unit to improve the efficiency of parameter auto-calibration and global sensitivity analysis. *Journal of Hydrology*, 598, 125726. <https://doi.org/10.1016/j.jhydrol.2020.125726>
- Christidis, N., Jones, G. S., & Stott, P. A. (2015). Dramatically increasing chance of extremely hot summers since the 2003 European heatwave. *Nature Climate Change*, 5(1), 46–50. <https://doi.org/10.1038/nclimate2468>
- Ciais, P., Reichstein, M., Viovy, N., Granier, A., Ogée, J., Allard, V., et al. (2005). Europe-wide reduction in primary productivity caused by the heat and drought in 2003. *Nature*, 437(7058), 529–533. <https://doi.org/10.1038/nature03972>
- Denissen, J. M. C., Teuling, A. J., Pitman, A. J., Koirala, S., Migliavacca, M., Li, W., et al. (2022). Widespread shift from ecosystem energy to water limitation with climate change. *Nature Climate Change*, 12(7), 677–684. <https://doi.org/10.1038/s41558-022-01403-8>
- Dickinson, R. E. (1983). Land surface processes and climate—Surface albedos and energy balance. In B. Saltzman (Ed.), *Advances in Geophysics* (Vol. 25, pp. 305–353). Elsevier. [https://doi.org/10.1016/S0065-2687\(08\)60176-4](https://doi.org/10.1016/S0065-2687(08)60176-4)
- Fel, T., Cadene, R., Chalvidal, M., Cord, M., Vigouroux, D., & Serre, T. (2021). Look at the variance! Efficient black-box explanations with sobol-based sensitivity analysis. In M. Ranzato, A. Beygelzimer, Y. Dauphin, P. S. Liang, & J. W. Vaughan (Eds.), *Advances in neural information processing systems* (Vol. 34, pp. 26005–26014). Curran Associates, Inc. Retrieved from <https://proceedings.neurips.cc/paper/2021/file/da94ceff56cfda50785df477941308b-Paper.pdf>
- Fischer, E. M., Seneviratne, S. I., Lüthi, D., & Schär, C. (2007). Contribution of land-atmosphere coupling to recent European summer heat waves. *Geophysical Research Letters*, 34(6). <https://doi.org/10.1029/2006GL029068>
- Gelaro, R., McCarty, W., Suárez, M. J., Todling, R., Molod, A., Takacs, L., et al. (2017). The modern-era retrospective analysis for research and applications, Version 2 (MERRA-2). *Journal of Climate*, 30(14), 5419–5454. <https://doi.org/10.1175/JCLI-D-16-0758.1>
- Gentine, P., Massmann, A., Lintner, B. R., Hamed Alejomahmad, S., Fu, R., Green, J. K., et al. (2019). Land–atmosphere interactions in the tropics—A review. *Hydrology and Earth System Sciences*, 23(10), 4171–4197. <https://doi.org/10.5194/hess-23-4171-2019>
- Gerken, T., Ruddell, B. L., Yu, R., Stoy, P. C., & Drewry, D. T. (2019). Robust observations of land-to-atmosphere feedbacks using the information flows of FLUXNET. *Npj Climate and Atmospheric Science*, 2(1), 1–10. <https://doi.org/10.1038/s41612-019-0094-4>
- Gershunov, A., Cayan, D. R., & Iacobellis, S. F. (2009). The great 2006 heat wave over California and Nevada: Signal of an increasing trend. *Journal of Climate*, 22(23), 6181–6203. <https://doi.org/10.1175/2009JCLI2465.1>
- Gillett, N. P., Stone, D. A., Stott, P. A., Nozawa, T., Karpechko, A. Y., Hegerl, G. C., et al. (2008). Attribution of polar warming to human influence. *Nature Geoscience*, 1(11), 750–754. <https://doi.org/10.1038/ngeo338>
- Hersbach, H., Bell, B., Berrisford, P., Hirahara, S., Horányi, A., Muñoz-Sabater, J., et al. (2020). The ERA5 global reanalysis. *Quarterly Journal of the Royal Meteorological Society*, 146(730), 1999–2049. <https://doi.org/10.1002/qj.3803>
- Hirsch, A. L., Evans, J. P., Di Virgilio, G., Perkins-Kirkpatrick, S. E., Argüeso, D., Pitman, A. J., et al. (2019). Amplification of Australian heatwaves via local land-atmosphere coupling. *Journal of Geophysical Research: Atmospheres*, 124(24), 13625–13647. <https://doi.org/10.1029/2019JD030665>
- Hochreiter, S., & Schmidhuber, J. (1997). Long short-term memory. *Neural Computation*, 9(8), 1735–1780. <https://doi.org/10.1162/neco.1997.9.8.1735>
- Hong, J.-S., Yeh, S.-W., & Seo, K.-H. (2018). Diagnosing physical mechanisms leading to pure heat waves versus pure tropical nights over the Korean Peninsula. *Journal of Geophysical Research: Atmospheres*, 123(14), 7149–7160. <https://doi.org/10.1029/2018JD028360>
- Horton, R. M., Mankin, J. S., Lesk, C., Coffel, E., & Raymond, C. (2016). A review of recent advances in research on extreme heat events. *Current Climate Change Reports*, 2(4), 242–259. <https://doi.org/10.1007/s40641-016-0042-x>
- Huang, J., Li, Y., Fu, C., Chen, F., Fu, Q., Dai, A., et al. (2017). Dryland climate change: Recent progress and challenges. *Reviews of Geophysics*, 55(3), 719–778. <https://doi.org/10.1002/2016RG000550>
- Jyoteeshkumar reddy, P., Sharples, J. J., Lewis, S. C., & Perkins-Kirkpatrick, S. E. (2021). Modulating influence of drought on the synergy between heatwaves and dead fine fuel moisture content of bushfire fuels in the Southeast Australian region. *Weather and Climate Extremes*, 31, 100300. <https://doi.org/10.1016/j.wace.2020.100300>
- Kang, S. M., Shin, Y., & Xie, S.-P. (2018). Extratropical forcing and tropical rainfall distribution: Energetics framework and ocean Ekman advection. *Npj Climate and Atmospheric Science*, 1(1), 1–10. <https://doi.org/10.1038/s41612-017-0004-6>
- Kautz, L.-A., Martius, O., Pfahl, S., Pinto, J. G., Ramos, A. M., Sousa, P. M., & Woollings, T. (2022). Atmospheric blocking and weather extremes over the Euro-Atlantic sector—A review. *Weather and Climate Dynamics*, 3(1), 305–336. <https://doi.org/10.5194/wcd-3-305-2022>

- Khan, M. I., & Maity, R. (2022). Hybrid deep learning approach for multi-step-ahead prediction for daily maximum temperature and heatwaves. *Theoretical and Applied Climatology*, 149(3), 945–963. <https://doi.org/10.1007/s00704-022-04103-7>
- Kobayashi, S., Ota, Y., Harada, Y., Ebina, A., Moriya, M., Onoda, H., et al. (2015). The JRA-55 reanalysis: General specifications and basic characteristics. *气象集誌. 第2輯*, 93(1), 5–48. <https://doi.org/10.2151/jmsj.2015-001>
- Kovats, R. S., & Hajat, S. (2008). Heat stress and public health: A critical review. *Annual Review of Public Health*, 29(1), 41–55. <https://doi.org/10.1146/annurev.publhealth.29.020907.090843>
- Kratzert, F., Klotz, D., Brenner, C., Schulz, K., & Herrnegger, M. (2018). Rainfall-runoff modelling using long short-term memory (LSTM) networks. *Hydrology and Earth System Sciences*, 22(11), 6005–6022. <https://doi.org/10.5194/hess-22-6005-2018>
- Lansu, E. M., van Heerwaarden, C. C., Stegehuis, A. I., & Teuling, A. J. (2020). Atmospheric aridity and apparent soil moisture drought in European forest during heat waves. *Geophysical Research Letters*, 47(6), e2020GL087091. <https://doi.org/10.1029/2020GL087091>
- Li, J., Tam, C.-Y., Tai, A. P. K., & Lau, N.-C. (2021). Vegetation-heatwave correlations and contrasting energy exchange responses of different vegetation types to summer heatwaves in the Northern Hemisphere during the 1982–2011 period. *Agricultural and Forest Meteorology*, 296, 108208. <https://doi.org/10.1016/j.agrformet.2020.108208>
- Li, Y., Ding, Y., & Li, W. (2017). Observed trends in various aspects of compound heat waves across China from 1961 to 2015. *Journal of Meteorological Research*, 31(3), 455–467. <https://doi.org/10.1007/s13351-017-6150-2>
- Liang, L., Yu, L., & Wang, Z. (2022). Identifying the dominant impact factors and their contributions to heatwave events over mainland China. *The Science of the Total Environment*, 848, 157527. <https://doi.org/10.1016/j.scitotenv.2022.157527>
- Liu, B., Lai, M., Zeng, P., & Chen, J. (2024). Air pollutant prediction based on a attention mechanism model of the Yangtze River delta region in frequent heatwaves. *Atmospheric Research*, 311, 107701. <https://doi.org/10.1016/j.atmosres.2024.107701>
- Luo, M., & Lau, N.-C. (2020). Summer heat extremes in northern continents linked to developing ENSO events. *Environmental Research Letters*, 15(7), 074042. <https://doi.org/10.1088/1748-9326/ab7d07>
- Luo, M., & Lau, N.-C. (2021). Increasing human-perceived heat stress risks exacerbated by urbanization in China: A comparative study based on multiple metrics. *Earth's Future*, 9(7), e2020EF001848. <https://doi.org/10.1029/2020EF001848>
- Luo, M., Lau, N.-C., & Liu, Z. (2022). Different mechanisms for daytime, nighttime, and compound heatwaves in southern China. *Weather and Climate Extremes*, 36, 100449. <https://doi.org/10.1016/j.wace.2022.100449>
- Luther, D. S., Harrison, D. E., & Knox, R. A. (1983). Zonal winds in the central equatorial Pacific and El Niño. *Science*, 222(4621), 327–330. <https://doi.org/10.1126/science.222.4621.327>
- Ma, F., Yuan, X., & Li, H. (2022). Characteristics and circulation patterns for wet and dry compound day-night heat waves in mid-eastern China. *Global and Planetary Change*, 213, 103839. <https://doi.org/10.1016/j.gloplacha.2022.103839>
- Ma, F., Yuan, X., Wu, P., & Zeng, Z. (2022). A moderate mitigation can significantly delay the emergence of compound hot extremes. *Journal of Geophysical Research: Atmospheres*, 127(2), e2021JD035427. <https://doi.org/10.1029/2021JD035427>
- Martens, B., Miralles, D. G., Lievens, H., van der Schalie, R., de Jeu, R. A. M., Fernández-Prieto, D., et al. (2017). GLEAM v3: Satellite-based land evaporation and root-zone soil moisture. *Geoscientific Model Development*, 10(5), 1903–1925. <https://doi.org/10.5194/gmd-10-1903-2017>
- McKay, M. D. (1988). Sensitivity and uncertainty analysis using a statistical sample of input values. *Uncertainty Analysis*, 145–186.
- McPhaden, M. J., Zebiak, S. E., & Glantz, M. H. (2006). ENSO as an integrating concept in Earth science. *Science*, 314(5806), 1740–1745. <https://doi.org/10.1126/science.1132588>
- Meehl, G. A., & Tebaldi, C. (2004). More intense, more frequent, and longer lasting heat waves in the 21st Century. *Science*, 305(5686), 994–997. <https://doi.org/10.1126/science.1098704>
- Miralles, D. G., Gentile, P., Seneviratne, S. I., & Teuling, A. J. (2019). Land–atmospheric feedbacks during droughts and heatwaves: State of the science and current challenges. *Annals of the New York Academy of Sciences*, 1436(1), 19–35. <https://doi.org/10.1111/nyas.13912>
- Miralles, D. G., Teuling, A. J., van Heerwaarden, C. C., & Vilà-Guerau de Arellano, J. (2014). Mega-heatwave temperatures due to combined soil desiccation and atmospheric heat accumulation. *Nature Geoscience*, 7(5), 345–349. <https://doi.org/10.1038/ngeo2141>
- Mizutori, M., & Guha-Sapir, D. (2017). *Economic losses, poverty and disasters 1998–2017* (Vol. 4, pp. 9–15). United Nations Office for Disaster Risk Reduction.
- Muñoz-Sabater, J., Dutra, E., Agustí-Panareda, A., Albergel, C., Arduini, G., Balsamo, G., et al. (2021). ERA5-Land: A state-of-the-art global reanalysis dataset for land applications. *Earth System Science Data*, 13(9), 4349–4383. <https://doi.org/10.5194/essd-13-4349-2021>
- Naud, C. M., Chen, Y., Rangwala, I., & Miller, J. R. (2013). Sensitivity of downward longwave surface radiation to moisture and cloud changes in a high-elevation region. *Journal of Geophysical Research: Atmospheres*, 118(17), 10072–10081. <https://doi.org/10.1002/jgrd.50644>
- O, S., & Orth, R. (2021). Global soil moisture data derived through machine learning trained with in-situ measurements. *Scientific Data*, 8(1), 170. <https://doi.org/10.1038/s41597-021-00964-1>
- Pan, Y., Wang, W., & Shi, W. (2019). Assessment of CPC global daily surface air temperature (CPC-T2m) analysis. *Assessment*, 22, 24.
- Parker, T. J., Berry, G. J., Reeder, M. J., & Nicholls, N. (2014). Modes of climate variability and heat waves in Victoria, southeastern Australia. *Geophysical Research Letters*, 41(19), 6926–6934. <https://doi.org/10.1002/2014GL061736>
- Park Williams, A., Allen, C. D., Macalady, A. K., Griffin, D., Woodhouse, C. A., Meko, D. M., et al. (2013). Temperature as a potent driver of regional forest drought stress and tree mortality. *Nature Climate Change*, 3(3), 292–297. <https://doi.org/10.1038/nclimate1693>
- Perkins, S. E., Argüeso, D., & White, C. J. (2015). Relationships between climate variability, soil moisture, and Australian heatwaves. *Journal of Geophysical Research: Atmospheres*, 120(16), 8144–8164. <https://doi.org/10.1002/2015JD023592>
- Perkins-Kirkpatrick, S. E., & Lewis, S. C. (2020). Increasing trends in regional heatwaves. *Nature Communications*, 11(1), 3357. <https://doi.org/10.1038/s41467-020-16970-7>
- Power, S. B., & Smith, I. N. (2007). Weakening of the Walker Circulation and apparent dominance of El Niño both reach record levels, but has ENSO really changed? *Geophysical Research Letters*, 34(18). <https://doi.org/10.1029/2007GL030854>
- Ren, Y., Wang, S., & Xia, B. (2023). Deep learning coupled model based on TCN-LSTM for particulate matter concentration prediction. *Atmospheric Pollution Research*, 14(4), 101703. <https://doi.org/10.1016/j.apr.2023.101703>
- Robinne, F.-N., Hallema, D. W., Bladon, K. D., & Buttle, J. M. (2020). Wildfire impacts on hydrologic ecosystem services in North American high-latitude forests: A scoping review. *Journal of Hydrology*, 581, 124360. <https://doi.org/10.1016/j.jhydrol.2019.124360>
- Röthlisberger, M., & Papritz, L. (2023). Quantifying the physical processes leading to atmospheric hot extremes at a global scale. *Nature Geoscience*, 16(3), 210–216. <https://doi.org/10.1038/s41561-023-01126-1>
- Russo, S., Sillmann, J., & Fischer, E. M. (2015). Top ten European heatwaves since 1950 and their occurrence in the coming decades. *Environmental Research Letters*, 10(12), 124003. <https://doi.org/10.1088/1748-9326/10/12/124003>

- Sato, K., & Simmonds, I. (2021). Antarctic skin temperature warming related to enhanced downward longwave radiation associated with increased atmospheric advection of moisture and temperature. *Environmental Research Letters*, 16(6), 064059. <https://doi.org/10.1088/1748-9326/ac0211>
- Schaller, N., Sillmann, J., Anstey, J., Fischer, E. M., Grams, C. M., & Russo, S. (2018). Influence of blocking on Northern European and Western Russian heatwaves in large climate model ensembles. *Environmental Research Letters*, 13(5), 054015. <https://doi.org/10.1088/1748-9326/aaaba5>
- Schumacher, D. L., Keune, J., & Miralles, D. G. (2020). Atmospheric heat and moisture transport to energy- and water-limited ecosystems. *Annals of the New York Academy of Sciences*, 1472(1), 123–138. <https://doi.org/10.1111/nyas.14357>
- Seneviratne, S. I., Corti, T., Davin, E. L., Hirschi, M., Jaeger, E. B., Lehner, I., et al. (2010). Investigating soil moisture-climate interactions in a changing climate: A review. *Earth-Science Reviews*, 99(3–4), 125–161. <https://doi.org/10.1016/j.earscirev.2010.02.004>
- Seneviratne, S. I., Lüthi, D., Litschi, M., & Schär, C. (2006). Land-atmosphere coupling and climate change in Europe. *Nature*, 443(7108), 205–209. <https://doi.org/10.1038/nature05095>
- Sheridan, S. C., Lee, C. C., & Smith, E. T. (2020). A comparison between station observations and reanalysis data in the identification of extreme temperature events. *Geophysical Research Letters*, 47(15), e2020GL088120. <https://doi.org/10.1029/2020GL088120>
- Shugar, D. H., Jacquemart, M., Shean, D., Bhushan, S., Upadhyay, K., Sattar, A., et al. (2021). A massive rock and ice avalanche caused the 2021 disaster at Chamoli, Indian Himalaya. *Science*, 373(6552), 300–306. <https://doi.org/10.1126/science.abh4455>
- Sobol', I. M. (2001). Global sensitivity indices for nonlinear mathematical models and their Monte Carlo estimates. *Mathematics and Computers in Simulation*, 55(1), 271–280. [https://doi.org/10.1016/S0378-4754\(00\)00270-6](https://doi.org/10.1016/S0378-4754(00)00270-6)
- Stephens, G. L., Wild, M., Stackhouse, P. W., L'Eucuyer, T., Kato, S., & Henderson, D. S. (2012). The global character of the flux of downward longwave radiation. *Journal of Climate*, 25(7), 2329–2340. <https://doi.org/10.1175/JCLI-D-11-00262.1>
- Stott, P. A., Stone, D. A., & Allen, M. R. (2004). Human contribution to the European heatwave of 2003. *Nature*, 432(7017), 610–614. <https://doi.org/10.1038/nature03089>
- Taylor, P. C., Cai, M., Hu, A., Meehl, J., Washington, W., & Zhang, G. J. (2013). A decomposition of feedback contributions to polar warming amplification. *Journal of Climate*, 26(18), 7023–7043. <https://doi.org/10.1175/JCLI-D-12-00696.1>
- Teuling, A. J., Seneviratne, S. I., Stöckli, R., Reichstein, M., Moors, E., Ciais, P., et al. (2010). Contrasting response of European forest and grassland energy exchange to heatwaves. *Nature Geoscience*, 3(10), 722–727. <https://doi.org/10.1038/ngeo950>
- Thirumalai, K., DiNezio, P. N., Okumura, Y., & Deser, C. (2017). Extreme temperatures in Southeast Asia caused by El Niño and worsened by global warming. *Nature Communications*, 8(1), 15531. <https://doi.org/10.1038/ncomms15531>
- Thomas, N. P., Bosilovich, M. G., Collow, A. B. M., Koster, R. D., Schubert, S. D., Dezfuli, A., & Mahanama, S. P. (2020). Mechanisms associated with daytime and nighttime heat waves over the contiguous United States. *Journal of Applied Meteorology and Climatology*, 59(11), 1865–1882. <https://doi.org/10.1175/JAMC-D-20-0053.1>
- Trenberth, K. E., Fasullo, J. T., & Kiehl, J. (2009). Earth's global energy budget. *Bulletin of the American Meteorological Society*, 90(3), 311–324. <https://doi.org/10.1175/2008BAMS2634.1>
- Vaidyanathan, A., Kegler, S. R., Saha, S. S., & Mulholland, J. A. (2016). A statistical framework to evaluate extreme weather definitions from a health perspective: A demonstration based on extreme heat events. *Bulletin of the American Meteorological Society*, 97(10), 1817–1830. <https://doi.org/10.1175/BAMS-D-15-00181.1>
- Wang, J., Chen, Y., Liao, W., He, G., Tett, S. F. B., Yan, Z., et al. (2021). Anthropogenic emissions and urbanization increase risk of compound hot extremes in cities. *Nature Climate Change*, 11(12), 1084–1089. <https://doi.org/10.1038/s41558-021-01196-2>
- Wang, J., Chen, Y., Tett, S. F. B., Yan, Z., Zhai, P., Feng, J., & Xia, J. (2020). Anthropogenically-driven increases in the risks of summertime compound hot extremes. *Nature Communications*, 11(1), 528. <https://doi.org/10.1038/s41467-019-14233-8>
- Wolter, K., & Timlin, M. S. (2011). El Niño/Southern Oscillation behaviour since 1871 as diagnosed in an extended multivariate ENSO index (MEI.ext). *International Journal of Climatology*, 31(7), 1074–1087. <https://doi.org/10.1002/joc.2336>
- Wouters, H., Keune, J., Petrova, I. Y., van Heerwaarden, C. C., Teuling, A. J., Pal, J. S., et al. (2022). Soil drought can mitigate deadly heat stress thanks to a reduction of air humidity. *Science Advances*, 8(1), eabe6653. <https://doi.org/10.1126/sciadv.abe6653>
- Wu, S., Luo, M., Zhao, R., Li, J., Sun, P., Liu, Z., et al. (2023). Local mechanisms for global daytime, nighttime, and compound heatwaves. *Npj Climate and Atmospheric Science*, 6(1), 1–13. <https://doi.org/10.1038/s41612-023-00365-8>
- Zhang, K. (2025). Global datasets of terrestrial daytime, nighttime, and compound heatwaves [Dataset]. National Tibetan Plateau/Third Pole Environment Data Center. <https://doi.org/10.11888/Atmos.tcdc.302636>
- Zhang, K., Li, X., Zheng, D., Zhang, L., & Zhu, G. (2022). Estimation of global irrigation water use by the integration of multiple satellite observations. *Water Resources Research*, 58(3), e2021WR030031. <https://doi.org/10.1029/2021wr030031>
- Zhou, S., & Yuan, X. (2023). Acceleration of the onset speeds of heat waves over East China by upwind flash droughts. *Journal of Geophysical Research: Atmospheres*, 128(10), e2022JD038072. <https://doi.org/10.1029/2022JD038072>
- Zhou, Y., Li, X., Zheng, D., Li, Z., An, B., Wang, Y., et al. (2021). The joint driving effects of climate and weather changes caused the Chamoli glacier-rock avalanche in the high altitudes of the India Himalaya. *Science China Earth Sciences*, 64(11), 1909–1921. <https://doi.org/10.1007/s11430-021-9844-0>
- Zou, J., Lu, N., Jiang, H., Qin, J., Yao, L., Xin, Y., & Su, F. (2022). Performance of air temperature from ERA5-Land reanalysis in coastal urban agglomeration of Southeast China. *The Science of the Total Environment*, 828, 154459. <https://doi.org/10.1016/j.scitotenv.2022.154459>
- Zscheischler, J., & Seneviratne, S. I. (2017). Dependence of drivers affects risks associated with compound events. *Science Advances*, 3(6), e1700263. <https://doi.org/10.1126/sciadv.1700263>

## References From the Supporting Information

- Beck, H. E., Zimmermann, N. E., McVicar, T. R., Vergopolan, N., Berg, A., & Wood, E. F. (2018). Present and future Köppen-Geiger climate classification maps at 1-km resolution. *Scientific Data*, 5(1), 180214. <https://doi.org/10.1038/sdata.2018.214>
- Martens, B., Waegeman, W., Dorigo, W. A., Verhoest, N. E. C., & Miralles, D. G. (2018). Terrestrial evaporation response to modes of climate variability. *Npj Climate and Atmospheric Science*, 1(1), 43. <https://doi.org/10.1038/s41612-018-0053-5>
- Nossent, J., Elsen, P., & Bauwens, W. (2011). Sobol' sensitivity analysis of a complex environmental model. *Environmental Modelling & Software*, 26(12), 1515–1525. <https://doi.org/10.1016/j.envsoft.2011.08.010>
- Rädel, G., Mauritsen, T., Stevens, B., Dommenget, D., Matei, D., Bellomo, K., & Clement, A. (2016). Amplification of El Niño by cloud longwave coupling to atmospheric circulation. *Nature Geoscience*, 9(2), 106–110. <https://doi.org/10.1038/ngeo2630>

- Sobol', I. M. (1993). Sensitivity estimates for nonlinear mathematical models. *Journal of Mathematical Modeling*, 2(1), 112–118.
- Soden, B. J. (2000). The sensitivity of the tropical hydrological cycle to ENSO. *Journal of Climate*, 13(3), 538–549. [https://doi.org/10.1175/1520-0442\(2000\)013<0538:TSOTTH>2.0.CO;2](https://doi.org/10.1175/1520-0442(2000)013<0538:TSOTTH>2.0.CO;2)
- Wang, B., & An, S. (2002). A mechanism for decadal changes of ENSO behavior: Roles of background wind changes. *Climate Dynamics*, 18(6), 475–486. <https://doi.org/10.1007/s00382-001-0189-5>